Kawada and Kasaya *Earth, Planets and Space (2018) 70:142*
https://doi.org/10.1186/s40623-018-0913-6

Earth, Planets and Space

FULL PAPER Open Access

Self-potential mapping using an autonomous underwater vehicle for the Sunrise deposit, Izu-Ogasawara arc, southern Japan

Yoshifumi Kawada[1,2*] and Takafumi Kasaya[2]

Abstract

We performed a simultaneous survey of self-potential and plume turbidity using an autonomous underwater vehicle (AUV) above the Sunrise deposit in the Myojin Knoll caldera of the Izu-Ogasawara arc. A 10-m-long electrode rod, on which five electrodes referenced with a common electrode were mounted, was connected at the tail of an AUV. The survey was conducted at a typical speed of 2 knots, covering the 1500 m × 1500 m area with a typical spacing of survey lines of 100 m. With AUV altitude of 100 m above the seafloor, a negative self-potential anomaly of a few millivolts was observed. The self-potential anomaly was found to spread 300 m × 300 m. The self-potential is probably attributable to the geo-battery mechanism: electric current is generated by redox reactions occurring around an ore body crossing a redox contrast. Assuming that the source of the self-potential is an electric current dipole, we can image a southward-dipping dipole with the moment of approximately 10^3 A m, approx. 30 m below the southern part of the ore deposit. Anomalies of turbidity, which are correlated to ambient temperature and which are signatures of discharged hydrothermal fluids, were distributed more broadly than the self-potential. Some turbidity anomalies were found without self-potential anomalies. They were probably transported by the ocean current. Spatial decoupling between the self-potential and turbidity anomalies suggests that the direct contribution of hydrothermal fluids to the self-potential anomalies is probably a secondary effect. The survey altitude of 100 m and the survey speed of 2 knots in the present study represent practical limitations for the self-potential survey when active hydrothermal fields are targeted. We have observed that the self-potential method responds exclusively to the presence of hydrothermal ore deposits. This behavior differs from other methods for exploring seafloor hydrothermal ore deposits: The geomagnetic method responds not only to ore deposits but also to volcanic bodies. The plume method can detect remote hydrothermal activities, but the source locations are not necessarily specified. The self-potential method is useful as an excellent exploration tool, particularly for initial surveys.

Keywords: Autonomous underwater vehicle (AUV), Hydrothermal ore deposits, Izu-Ogasawara arc, Marine self-potential method, Mineral exploration, Wide-area survey

*Correspondence: kawada@irides.tohoku.ac.jp
[1] International Research Institute of Disaster Science, Tohoku University, 468-1 Aoba, Aoba-ku, Sendai 980-0845, Japan
Full list of author information is available at the end of the article

Introduction

For the exploration of submarine hydrothermal ore deposits over wide areas, efficiency is crucially important (e.g., Yoerger et al. 2007). Geophysical mapping methods, which continuously observe signals away from the seafloor, might be the best choice for this purpose. Using a deep-towed array, we have demonstrated that the self-potential method, which measures in situ electrostatic potential (e.g., Jouniaux and Ishido 2012; Revil and Jardani 2013), works effectively to locate seafloor hydrothermal ore deposits (Kawada and Kasaya 2017). The observed self-potential signals are likely to detect redox reactions occurring around an ore body as a negative self-potential anomaly above it (Sato and Mooney 1960). The self-potential method is particularly efficient in marine environments because towing two or more non-polarized electrodes reveals in situ electrostatic fields. Although this method is not used very commonly in marine environments at present, it has been investigated continually since the 1970s (e.g., Beltenev et al. 2009; Brewitt-Taylor 1975; Cherkashev et al. 2013; Constable et al. 2018; Corwin 1976; Francis 1985; Heinson et al. 1999, 2005; Kawada and Kasaya 2017; Petersen and Shipboard Scientific Party 2016; Safipour et al. 2017; Von Herzen et al. 1996). The use of autonomous underwater vehicles (AUVs) greatly improves the efficiency of the self-potential survey (Constable et al. 2018; Sato et al. 2017). Sato et al. (2017) only measured self-potential. Constable et al. (2018) conducted combined observations of self-potential and electromagnetic surveys. The main purpose of the present study is to map the difference in response between self-potential and turbidity using this high efficiency.

The salient benefit of the self-potential method in marine environments is that it responds specifically to the presence of hydrothermal deposits, which is a unique feature that is unavailable from other geophysical methods. For instance, the geomagnetic method (e.g., Caratori Tontini et al. 2012a, b; Fujii et al. 2015; Gee et al. 2001; Honsho et al. 2013, 2016a, b; Szitkar et al. 2014a, b; Tivey and Dyment 2013; Tivey and Johnson 2002), which is regarded as an important method for exploring marine hydrothermal ore deposits (e.g., Urabe et al. 2015), responds to any magnetized/less-magnetized body. Actually, the observed magnetization is high (e.g., Gee et al. 2001; Honsho et al. 2016b) or low (e.g., Honsho et al. 2016a) depending on the mineral assemblage (e.g., Körner 1994) as well as the degree of hydrothermal alteration. Consequently, this method requires geological information about the target area. As another example, the plume survey method (e.g., Baker et al. 2005; German et al. 2008), which is used to explore active hydrothermal fields, responds to signatures of plume fluids. The fluid discharge location is sometimes different from the plume fluid location. Therefore, the discharge cannot always be specified. Self-potential signals are probably related more directly to the presence of ore deposits via the geo-battery mechanism.

Using a middle-class AUV, *Jinbei* (Hyakudome et al. 2012), we apply the self-potential method to a known Kuroko-type submarine hydrothermal ore deposit, the Sunrise deposit, which is associated with the Myojin Knoll caldera in the Izu-Ogasawara arc, southern Japan (Fig. 1) (Iizasa et al. 1999). Earlier studies have demonstrated that the use of an AUV can yield information related to hydrothermal ore deposits more efficiently than deep-towed arrays can (Constable et al. 2018; Sato et al. 2017). In this study, we extend our research to observe turbidity, which is evidence of discharged plume fluids, and to observe self-potential signals, which might originate directly from ore deposits below the seafloor. Furthermore, observed self-potential data are analyzed to obtain the intensity and polarization of an electric current dipole generated by the geo-battery. Finally, we compare the self-potential method to geomagnetic and plume survey methods. In short, self-potential signals yield more specific information than other passive methods do.

Geological background of the target area

The target area of this study, Myojin Knoll, is located in the Izu-Ogasawara arc, southern Japan (Fig. 1). The arc consists of a chain of arc volcanoes associated with subduction of the Pacific Plate into the Philippine Sea Plate from the east (Tamura and Tatsumi 2002; Tamura et al. 2009). Basaltic and rhyolitic volcanoes are located alternately from north to south along the arc (Tamura et al. 2009) (Fig. 1a). Myojin Knoll is a rhyolitic volcano with a caldera structure located in the middle part of the volcanic chain. The caldera (Fig. 1b) is an oval with the major axis extending in the E–W direction (7 km × 6 km). The caldera wall has height of 500–1000 m. The caldera floor comprises rhyolitic pumice underlain by rhyolitic lava, identified both by visual (Fiske et al. 2001) and seismic (Tsuru et al. 2008) surveys. Such layered structures are occasionally encountered in rhyolitic volcanoes (e.g., Urabe et al. 2005). The age of caldera collapse is unknown but it is assumed to be very young (several 1000 years) from a morphological perspective (Fiske et al. 2001). A rhyolitic lava dome with relative height of 350 m from the caldera floor is situated near the center of the caldera (Fig. 1b). The caldera wall is steep near the limb, but gentle near the foot.

The Sunrise deposit is located near the southeastern foot of the caldera wall near a scarp structure (Fig. 1c) (Iizasa et al. 1999) at water depth of 1200–1400 m. A

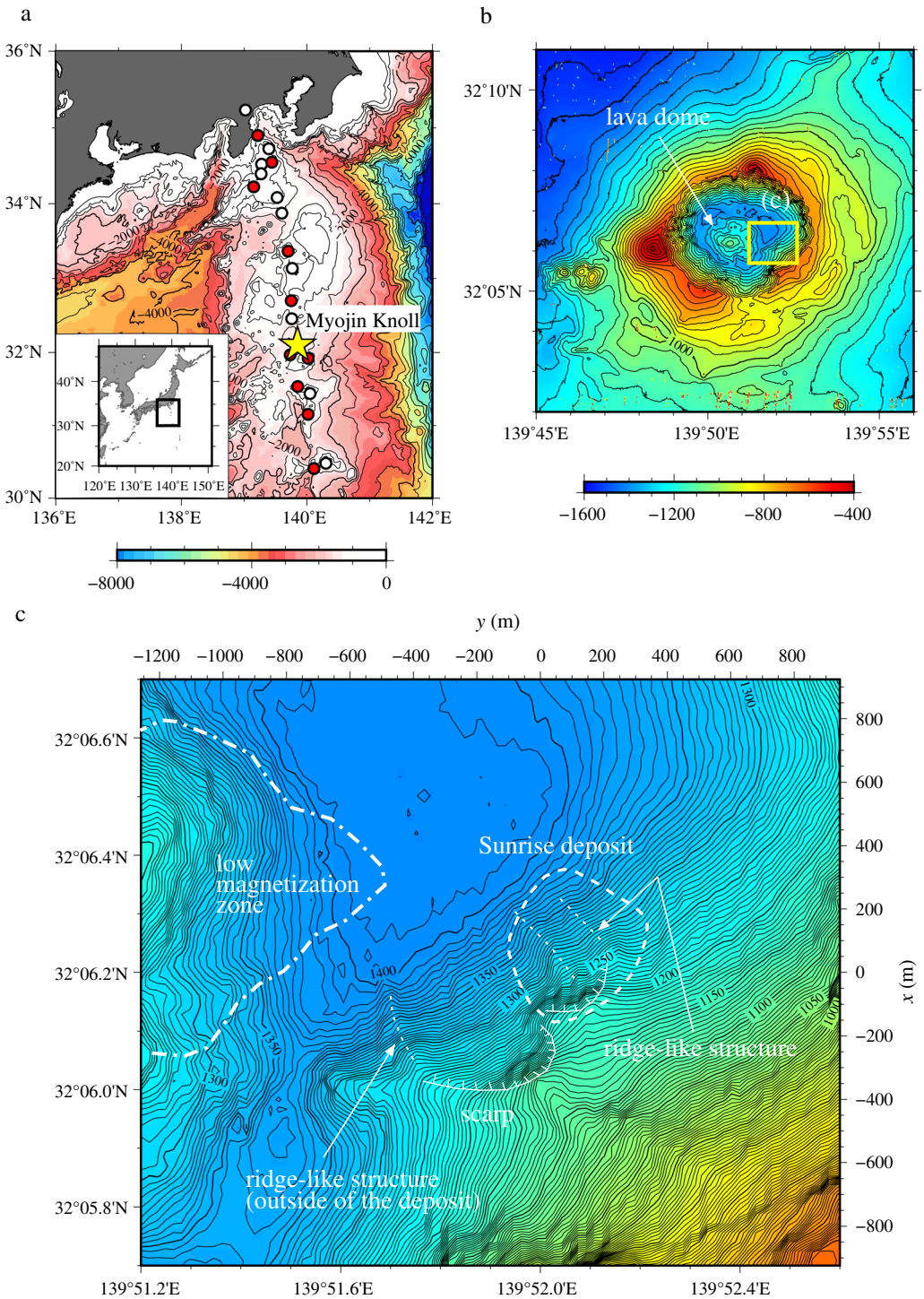

Fig. 1 Map of the target area. **a** Location of Myojin Knoll caldera in the Izu-Ogasawara arc, with the inset showing the location of the Japanese Islands. The white and red circles, respectively, denote the locations of basaltic and rhyolitic volcanoes (Tamura et al. 2009). The yellow star denotes the location of Myojin Knoll caldera (a rhyolitic volcano). **b** Plan view of Myojin Knoll caldera. The yellow box denotes the survey area of the present study shown in (c). The color scale is explained in the legend below. **c** Magnified plan view of the survey area. The color scale is the same as (**b**). The location of the Sunrise deposit (Iizasa et al. 1999) is marked by the thick dashed curve. The locations of a low-magnetization area, ridge-like structures, and scarp structures (Honsho et al. 2016a) are marked, respectively, by a dot-dashed curve, thin dotted curves, and inverted Ts

visual survey conducted using a submersible (Iizasa et al. 1999) approximated the deposit size as 400 m × 400 m. The mineral assemblage of this deposit is classified as Kuroko type: recovered samples consist of Cu–Zn–Pb sulfides with high Ag (approx. 1200 ppm) and Au (approx. 50 ppm) contents, which are, respectively, 24 and 40 times those taken from typical samples of Kuroko deposits (Iizasa et al. 1999). Iizasa et al. (1999) identified the hydrothermal vents discharging high-temperature fluids as aligned in the NW–SE direction. In the late 1990s, active hydrothermal vents discharging high-temperature fluids up to approx. 280 °C were recorded, but most (approx. 70%) observed vents were dead according to Iizasa et al. (1999), which led them to infer that this hydrothermal site was in a decline stage at that time. Later, in 2014, an acoustic survey detected signals of fluid discharge above the deposit (Honsho et al. 2016a). The system remained active in 2014.

Results of a detailed morphological survey using acoustic sounding suggest that the Sunrise deposit was formed in association with post-caldera volcanism that occurred after the main caldera collapse (Honsho et al. 2016a): ridge-like volcanic structures cut the caldera wall. Three ridge-like structures of post-caldera volcanism origin run along the NW–SE orientation inside of the Sunrise deposit (Honsho et al. 2016a). They are correlated with the distribution of hydrothermal vents found by Iizasa et al. (1999); the most active vent, designated as *Daimyo-jin*, is located near the southern end of the westernmost ridge. Two of the ridge-like structures are identifiable inside of the deposit from a bathymetry map compiled based on results of multi-beam sounding obtained during the cruise YK16-10 (Fig. 1c). A magnetic survey conducted using an AUV revealed that the Sunrise deposit shows a very weak low-magnetic anomaly, accompanied by an area with more intense magnetic low to the west of the deposit (Honsho et al. 2016a). Honsho et al. (2016a) reported that the discharge of high-temperature fluids along fractures of the caldera limb demagnetized host rocks by alteration, resulting in the formation of this low-magnetization zone, similarly to the Sunrise deposit.

Observation

Equipment

We used the AUV *Jinbei* (Hyakudome et al. 2012) (Fig. 2a), operated by *R/V Kaimei* of *the Japan Agency for Marine–Earth Science and Technology* (JAMSTEC), to demonstrate the effectiveness of AUVs for the

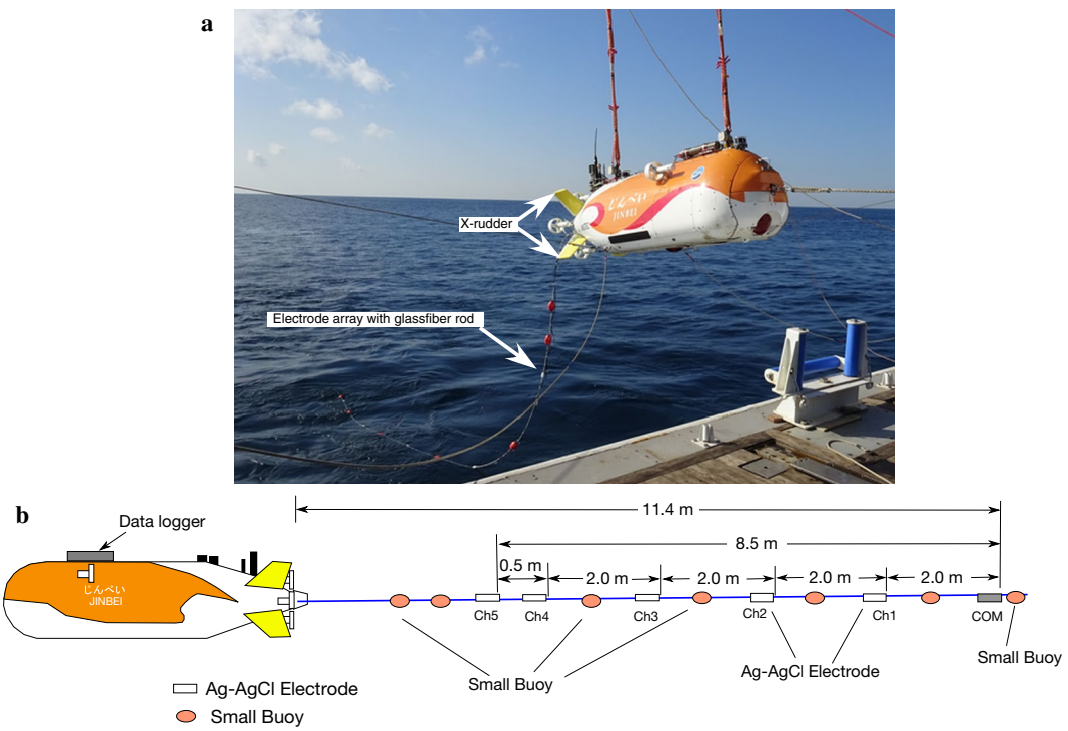

Fig. 2 Apparatus used in the present study. **a** Photograph of the side-view of the AUV *Jinbei* (Hyakudome et al. 2012). **b** Configuration of the present survey with a 10-m-long FRP electrode rod. Open squares on the cable show locations of five Ag/AgCl electrodes. The solid square is that of a reference (common) Ag/AgCl electrode. Orange ellipsoids show the locations of small plastic buoys to keep the rod neutral. The data logger is mounted outside of the AUV

exploration of hydrothermal deposits. *Jinbei* is a middle-class cruising-type AUV with maximum working depth of 3000 m. The 4-m-long, 1.1-m-wide, and 1.0-m-high vehicle has aerial weight of about 2 tons. It can cruise at 2–2.5 knots using four rear thrusters. The vehicle altitude can be controlled precisely by two azimuth thrusters mounted on the mid-ship of the body and by 'X' rudders on the rear. The AUV position is monitored in a three-dimensional space using a super-short baseline (SSBL) acoustic system (13–15 kHz range) and by an inertial navigation system (INS) with a Doppler velocity log (DVL) of 300 kHz. The vehicle is equipped with multiple environmental sensors including a hybrid pH–CO_2 sensor, a conductivity-temperature-depth (CTD) meter, a dissolved oxygen (DO) sensor, and a fluorescent turbidimeter. The vehicle is also equipped with an acoustic sounder, which is chosen exclusively from a multi-beam echo sounder or a side-scan sonar because of the load capacity.

For the self-potential survey, the AUV is equipped with a 10-m-long fiber-reinforced plastic (FRP) rod at the tail of the vehicle, on which five non-polarized Ag/AgCl electrodes (Filloux 1987) are mounted (Fig. 2b). These electrodes are referenced to a common electrode mounted near the tail of the rod. The number of independent signals is thereby five. The electrode distance is mainly 2 m, but it is 0.5 m at the AUV side. Raw data, electrostatic potentials among the five electrodes relative to the common electrode, are recorded using a high-precision (24 bit) multi-channel voltmeter, which was designed originally as a receiver unit of an active electromagnetic survey system (Goto et al. 2013).

Survey summary

Using the apparatus explained above, we conducted a self-potential survey covering the Sunrise deposit (Iizasa et al. 1999) during the KM16-10 cruise (see Additional file 1: Fig. A1 for raw data and Fig. A2 dive tracks), which was the first attempt for *Jinbei* to be engaged in scientific research. The survey was administered with a single dive during the daytime (Additional file 1: Fig. A1). The survey consists of two groups of survey lines, both of which cover an area of the Sunrise deposit (Figs. 1c and 3a; Additional file 1: Fig. A2). The eight survey lines in the first group (Lines 1–8) run in a NE–SW direction, sub-parallel to the depth contours of the caldera wall. The other four lines in the second group (Lines 9–12) run in an E–W direction, extending west of the deposit, where a low-magnetic anomaly was observed and interpreted as a fluid conduit (Honsho et al. 2016a). The survey height was 100 m on average, but it varied: 60–140 m. The survey was administered at approx. 2 knots. Sampling rates of instruments were 1 s, except for the SSBL, which was 8 s.

Two more survey lines (Lines S1 and S2), arranged in an E–W direction, are not addressed in this study because they are duplicated by some lines of the second group (Additional file 1: Fig. A2). The results of both sets are fundamentally the identical (Additional file 1: Fig. A3).

Data analysis

The time series of the horizontal position of the AUV is approximated from SSBL data using least-squares method (using a third-order polynomial) because the acoustic data are sometimes affected by scattering and a lack of data (Additional file 1: Figs. A2, A3). Moreover, the sampling rate is lower than those of other data. The AUV position estimated using INS is not used for this analysis because it is deviated via the time integration process. We assume that the electrode rod is parallel to the horizon because we did not measure the angle in the present survey. It is the cosine of the rod angle affecting estimation of the electric field. The angle is 20 deg at most (Kawada and Kasaya 2017). Consequently, the underestimation is approx. 6% in the worst case ($\cos(20°) \approx 0.94$). Neglecting the cable angle does not strongly affect the analysis results.

Raw data for the time series of the electrostatic potential of each sensor relative to the common electrode are processed in the following manner. First, outliers are removed from the data using a robust Kalman filter (RKF) with the Wiener filter (e.g., Kaneda et al. 2012). The RKF parameters are obtained by minimizing Akaike's information criterion (AIC) (e.g., Kitagawa 1993). Second, using linear least-squares fitting, constant and linear components are removed from the RKF processed time series. At this stage, any combination of two electrodes gives the electric field parallel to the electrode rod when divided by the sensor distance (see Fig. 2b). However, results demonstrate that Ch. 1 and 3 include more noise than other channels throughout the survey. Moreover, Ch. 3 shows large drift (Additional file 1: Fig. A1); we therefore decide not to use these channels for analyses. Third, we take an average of Ch. 2, 4, and 5 to obtain the electric field at each time. Finally, the electric field can be integrated along a survey line to ascertain the *effective* self-potential. This figure is not exact because the survey depth was not always constant. Moreover, the electrode rod might not be horizontal. Therefore, it is labeled as *effective*, but integration can produce a reasonable picture for practical purposes such as identifying the locations of self-potential anomalies.

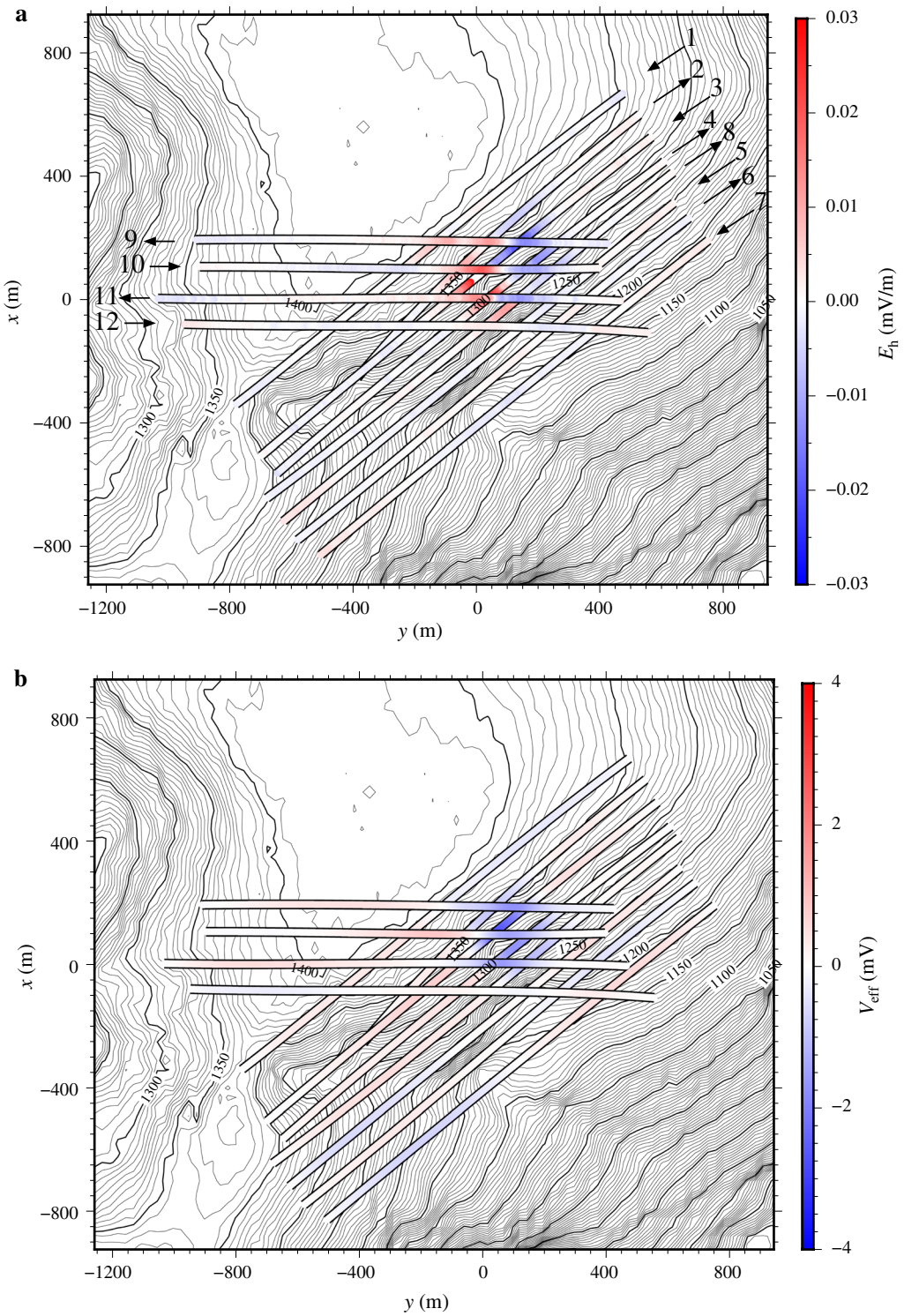

Fig. 3 Plan views of results relative to the origin point (32°06.2′N, 139°52.0′E): **a** Electric field along the dive track and **b** *effective* self-potential. The color scale is explained in the legend at the right of each panel. Numbers in **a** correspond to the dive tracks, with arrows denoting the survey direction. The dive tracks are basically located in ascending order except for Line 8, which is located between Lines 4 and 5. The polarization of some electric field data in **a** is inverted so that the survey direction is assumed to be from southwest to northeast (for Lines 1–8) or from west to east (for Lines 9–12)

Results

The electric field shows anomalies with amplitude of < 0.04 mV/m around the Sunrise deposit (Iizasa et al. 1999) (x of approx. −100 between 300 m and y of approx. −100 between 300 m in Fig. 3a; Fig. 1c presents the deposit location) with a survey height of approx. 100 m. No strong self-potential anomaly was found outside of the Sunrise deposit. The origin point (32°06.2′N, 139°52.0′E) was chosen near the center of the deposit. Integrating the electric field along the survey lines produces a circular negative (effective) self-potential anomaly with amplitude of a few millivolts (Fig. 3b). The area of the observed self-potential anomaly is approximated to 300 m × 300 m in the present survey (Fig. 3b), which is smaller than that reported by Iizasa et al. (1999) based on visual surveys, 400 m × 400 m (Fig. 1c). This difference appears to be reasonable because Iizasa et al. (1999) included not only the area of hydrothermal mounds of sulfides; they also included hydrothermal alteration zones.

Self-potential anomalies were detected along almost all survey tracks showing systematic variation in terms of the distance from the center of the deposit (Figs. 4, 5). For the first group of survey lines aligned NE–SW (Lines 1–8; see Fig. 3a for the location), only a very weak (Line 1; Fig. 4a) or no self-potential (Lines 5–7; Fig. 4f–h) anomaly was observed along the survey lines crossing the edge of the deposit. By contrast, a negative self-potential anomaly of a few millivolts was found along the lines crossing the center of the deposit (Lines 2–4, and 8; Fig. 4b, e). The horizontal coordinate of Lines 1–8 (x', y') is rotated 39° counterclockwise about the origin point relative to the original northing–easting coordinate (x, y) because the survey direction of these eight lines is running at about N51°E. The second group of E–W survey lines (Lines 9–12; see Fig. 3a for the location) exhibits similar characteristics (Fig. 5). These two groups of survey lines with different AUV headings yield almost identical results.

The observed self-potential shows asymmetries along the survey lines (e.g., Fig. 4c, d); these asymmetries are clearer in the electric field. Assuming that the source of the self-potential anomaly is an electric current dipole (Revil et al. 2001), we might image an inclined dipole. This possibility is evaluated in the next section by modeling the observed electric field. The observed self-potential (electric field) data also show small-scale fluctuations along four survey lines. Three of them (y' of approximately 100 m along Lines 3, 4, and 8; See Fig. 4c, e) are located near the center of the ore deposit, the location of which coincides with the eastern ridge-like structure observed by Honsho et al. (2016a); the other one ($y \sim 100$ m along Line 9; Fig. 5a) is near the northeastern edge of the ore deposit, the location of which coincides with the western ridge-like structure (see Fig. 1c for the location of the ridges). A side-scan survey detected a hydrothermal plume-like structure above these ridge-like structures (Honsho et al. 2016a), indicating that the observed fluctuations are related to the location of active hydrothermal vents.

Anomalies of turbidity were detected covering the area of the Sunrise deposit (Fig. 6). Two areas of intense turbidity anomalies were identified. First, a turbidity anomaly immediately above the Sunrise deposit is associated with large-scale self-potential anomalies (Lines 2–4, and 8 in Fig. 4b, e, Lines 9–11 in Fig. 5a, c). The most intense turbidity anomaly, observed above the southern part of the deposit, is consistent with earlier observations of active vents at the southern part of the deposit (Honsho et al. 2016a; Iizasa et al. 1999). The self-potential anomaly is circular, as described above, probably reflecting the distribution of the ore deposit. Second, by contrast, turbidity anomalies found above the areas west (x of approx. −100 m and y of approx. −400 m; Line 12; Fig. 5d) and northeast (x of 100–500 m and y of 200–400 m; Lines 5 and 6; Fig. 4f, g) of the deposit are not accompanied by the self-potential anomaly (compare Fig. 3b with 6). The second turbidity anomalies seem to spread along the depth contour lines (Fig. 6), which might be branched from the intense turbidity anomalies influenced by the ambient ocean current.

Anomalies of ambient temperature and salinity (calculated from temperature, pressure, and electrical conductivity of the CTD data using an empirical relation) were observed at similar locations of turbidity anomalies, but they are not always correlated with turbidity. For example, a turbidity anomaly detected around y of approx. −350 m along Line 12 is not accompanied by temperature and salinity anomalies (Fig. 5d). Temperature and salinity are mutually correlated: they show anomalies above the Sunrise deposit (Lines 2–4, and 8; Fig. 4b, e) and above the areas west (Lines 5 and 6; Fig. 4f, g) and northeast (Lines 10 and 11; Fig. 5b, c) of the deposit. However, the water depth was found to vary among the survey tracks in this study because the Sunrise deposit is distributed on the caldera wall (water depth between 1200 and 1400 m). The anomalies of temperature and salinity, which depend on water depth, cannot be constrained very well.

Modeling

To estimate the location and polarization of the electric current source generated by the geo-battery, we apply the probability tomography method (Patella 1997a, b; Revil et al. 2001) and the point source inversion to the observed electric field data. Assuming that the source is

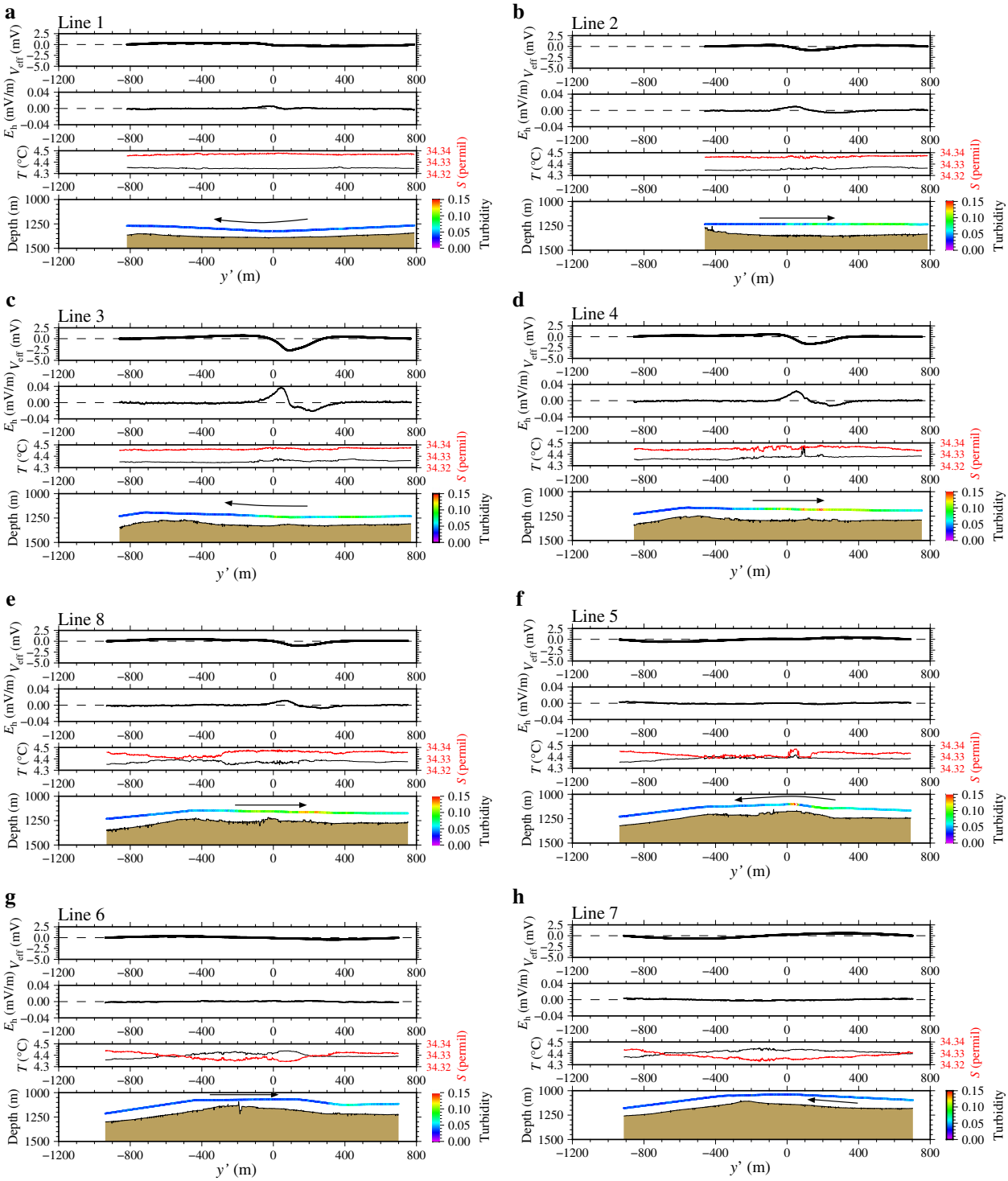

Fig. 4 Cross-sectional view of the results along selected survey lines directing NE–SW: **a**–**h** correspond to Lines 1–4, 8, 5–7 from northwest to southeast. Line numbers correspond to those in Fig. 3a. The horizontal coordinate is rotated 39° counterclockwise with respect to the origin point (32°06.2′N, 139°52.0′E) because the survey direction is approx. N51°E: (upper panel) effective self-potential; (upper middle panel) electric field along the dive track; (lower middle panel) ambient temperature (black curve, left axis) and salinity (red curve, right axis); and (lower panel) AUV depth with turbidity (upper curves; color scale is shown at the right), water depth (top of the brown area), and the survey direction (arrow). The water depth is calculated by summing the AUV depth and altitude

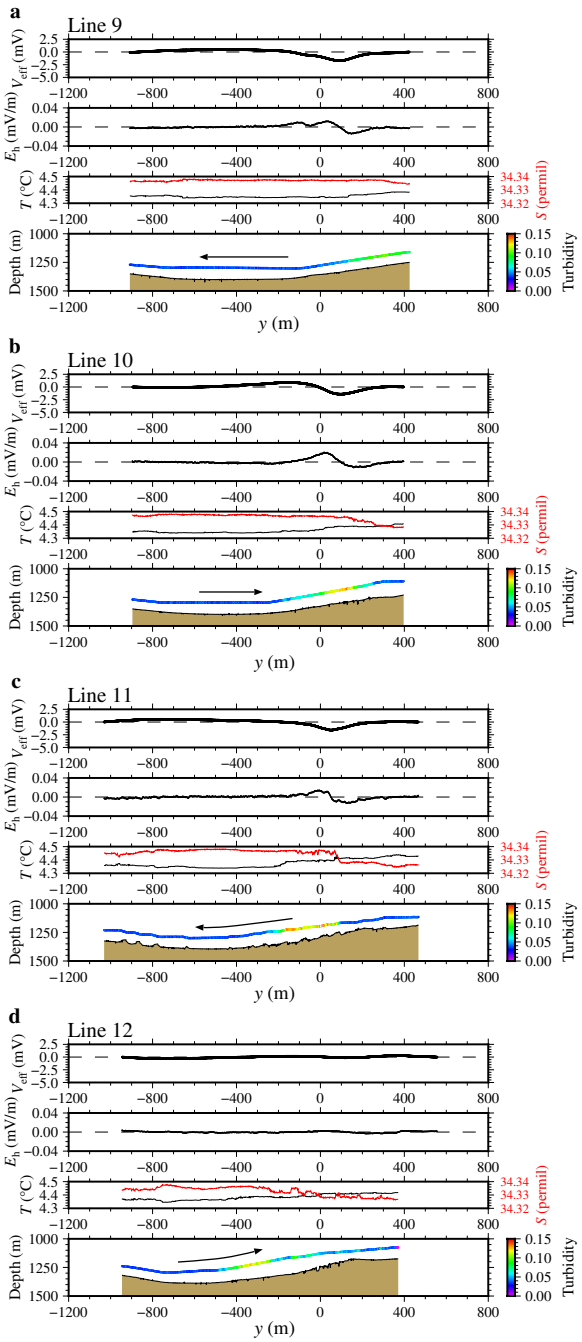

Fig. 5 Cross-sectional view of the results along selected survey lines directing E–W: **a**–**d** correspond to Lines 9–12 from north to south. Line numbers correspond to those in Fig. 3a. The horizontal coordinate is easting with respect to the origin point (139°52.0′E), along which the observation was conducted. The notation follows that presented in Fig. 4

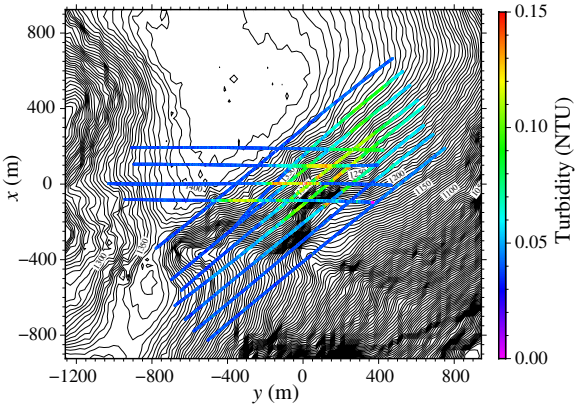

Fig. 6 Plan views of the observed turbidity relative to the origin point (32°06.2′N, 139°52.0′E). The color scale meaning is explained in the legend at the right of the panel

a point-wise electric current dipole (Revil et al. 2001), the probability tomography method takes a cross-correlation between the electric field generated by a synthetic electric current dipole (of a unit dipole moment) and the observed one. Assuming also that the source is a point-wise electric current dipole, the point source inversion minimizes the misfit between the electric field generated by a synthetic electric current dipole and that observed. Here we intend to estimate the dipole location, strength, and polarization at a first order. Solving a full inversion problem using either a deterministic (e.g., Minsley et al. 2007) or stochastic (e.g., Jardani and Revil 2009) framework is not conducted. The reader might refer to Revil and Jardani (2013) for an extensive review for the inverse problem.

To apply the probability tomography method, we compare the observed electric field with the electric fields induced by three synthetic dipoles whose polarization is parallel to one of the coordinate axes. Each component of the resulted polarization vector is assumed to be proportional to the probability for the corresponding synthetic dipole. The intensity is assumed to be proportional to the norm of the polarization vector. The source location is assumed to be the point where the intensity takes an extreme value. The dipole estimated by the probability tomography is not the best fit result. Therefore, we subsequently apply the point source inversion. The number of unknowns for the point source inversion is six: the dipole position and the polarization vector. The dipole moment is the norm of the resultant polarization vector. The objective function is minimized using the standard Newton–Raphson method. We found that the inversed result is robust for the choice of initial conditions. In both analyses, the observed electric field is assumed to be parallel to the survey line in the horizontal direction with a zero vertical component because we only observed the electric field along the towed rod (Fig. 2b). We incorporate Lines 1–12 into analysis and specify the source

location and polarization in the three-dimensional space. Although this method does not include the effects of electrical conductivity contrast, we have demonstrated that it does not greatly affect the estimated source depth (< 10 m) in the presence of electrical conductivity contrast (Kawada and Kasaya 2017). The result is useful for a first-order approximation.

We can roughly estimate the polarization vector intensity in the presence of electrical conductivity contrast. In the absence of topography, we can incorporate the electrical conductivity contrast effects using an analytical solution for the electric field in the ocean induced by a point-wise electric current dipole buried in the sediment layer:

$$\vec{E} = \frac{1}{4\pi\sigma_{\mathrm{sed}}}\left(1-\frac{\sigma_{\mathrm{sw}}-\sigma_{\mathrm{sed}}}{\sigma_{\mathrm{sw}}+\sigma_{\mathrm{sed}}}\right)\left\{\frac{3\vec{P}\cdot(\vec{r}-\vec{r}_s)}{|\vec{r}-\vec{r}_s|^5}(\vec{r}-\vec{r}_s)-\frac{1}{|\vec{r}-\vec{r}_s|^3}\vec{P}\right\}, \tag{1}$$

Using the point source inversion, the dipole source is estimated below the southern part of the ore deposit ($x = 20$ m, $y = 90$ m, and $z = -1310$ m) (Fig. 7; for the fitting, see Additional file 1: Figs. A4 and A5), the location of which is near the most active hydrothermal vent called *Daimyojin* (Iizasa et al. 1999). The source depth is estimated at approximately 30 m below the seafloor. This result suggests the existence of a shallow ore deposit, considering the wide horizontal spreading of the deposit, 400 m × 400 m (Iizasa et al. 1999). The estimated dipole polarization is southward in the horizontal direction, with a dip angle of approx. 60° from the vertical direction. This inclination reflects asymmetries in the observed electric field (e.g., Fig. 4c). Probability tomography yields a similar result, although it gives a more steep dipole, with the dip angle of approx. 45° from the vertical. Results of probability tomography are presented elsewhere (Additional file 1: Fig. A6).

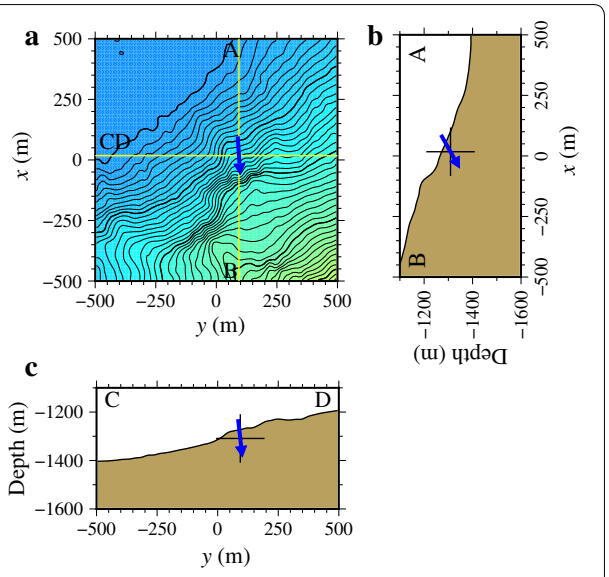

Fig. 7 Result of point source inversion. **a** Map view of the polarization vector with the bathymetry. Two cross sections displayed in **b** and **c** are shown by the yellow lines. The blue arrow is the horizontally projected polarization vector. **b** Polarization vector projected along the cross section A–B and **c** that along the cross section C–D in **a**: the polarization is shown by the blue arrow

where $\vec{r}$ and $\vec{r}_s$, respectively, represent the observed and source locations, $\vec{P}$ is the polarization vector, and σ_{sw} (3 S/m) and σ_{sed} (variable but around 1 S/m near the seafloor), respectively, denote the electric conductivities of seawater and sediment. By incorporating the effects of sediment conductivity, when a signal is observed in the seawater, the dipole moment from a dipole buried in the sediment layer is two-third of that from the corresponding dipole in an infinite seawater layer. We use Eq. (1) in the presence of topography as a first-order approximation. The resultant electric current dipole moment is approximately 1.4×10^3 A m. Probability tomography gives the dipole moment of approx. 1.3×10^3 A m by matching the amplitudes of the synthetic and observed electric fields and using Eq. (1). This estimation is probably the first-time result for the dipole moment of an electric current source for an ore deposit associated with a high-temperature hydrothermal system. Constable et al. (2018) estimated the source intensity assuming subsurface monopole current sources with total intensity of zero.

The existence of a southward inclined dipole might reflect the sub-seafloor structure of the Sunrise deposit. This deposit might be influenced by fracture-restricted or fault-restricted fluid flow related to caldera formation activity, as was the Hakurei deposit on the Bayonnaise caldera (Honsho et al. 2013), 20 km southeast of the Myojin caldera (Fig. 1a), rather than being formed by simple upwelling fluid flow like the TAG mound on the Mid-Atlantic Ridge (e.g., Hannington et al. 1998). A seismic study of the Bayonnaise caldera revealed fractures pervasively distributed inside of the caldera rim (Yamashita et al. 2015). Yamashita et al. (2015) postulated that these fractures induce fluid flow outside of the caldera rim. Further studies might elucidate the hydrological structure including this type of caldera-scale fluid flow that forms the Sunrise deposit.

Finally, we emphasize the importance of the three-dimensional analysis demonstrated here, which is crucially important for imaging a correct dipole polarization.

For 2.5-dimensional analyses using data of each single survey line with an assumption that the survey track is a straight line, the source is immediately below it, and the polarization vector is restricted to the vertical plane below it, we find a different dipole polarization (Additional file 1: Fig. A7). Every NE–WS survey line predicts a southwestward-dipping dipole; every E–W survey line predicts an eastward-dipping dipole. However, the polarization of the three-dimensional analysis falls between those of the 2.5-dimensional analysis. The estimated dipole moment varies from 1.0×10^3 to 1.6×10^3 A m, which also falls between those of the 2.5-dimensional analysis.

Discussion

The present cruise produced a map of self-potential anomalies above a known hydrothermal ore deposit using an AUV with survey height of about 100 m (Figs. 3b, 4, 5). This map depicts a negative anomaly of a few millivolts spreading 300 m × 300 m. This cruise demonstrates that no complicated data analysis is necessary merely to specify the deposit location. The resultant self-potential signals are higher than the detection limit, even at the survey height of approx. 100 m. This survey height might represent a practical upper limit for exploring hydrothermal deposits with hydrothermal activities. Less active systems might require lower survey altitudes (approx. 5–10 m) (e.g., Heinson et al. 1999, 2005; Safipour et al. 2017).

Self-potential method as an excellent exploration tool for initial surveys

Self-potential method obviates complicated data analysis, making it ideal for the efficient exploration of ore deposits. In fact, it requires no detailed geological information for interpretation. This benefit reflects the fact that the self-potential signals are linked directly to physicochemical processes that are inherent to ore deposits. The geo-battery is the most plausible mechanism for self-potential signals emerging near ore bodies (Sato and Mooney 1960): an electrically conductive body (an ore deposit) in the presence of subsurface redox gradient produces a negative self-potential anomaly above it. The geo-battery mechanism is not expected to work near less-conductive volcanic bodies. An earlier report described that no self-potential anomaly was actually observed above volcanic bodies (Kawada and Kasaya 2017). This behavior prevents unnecessary explorations conducted for an earlier study (e.g., Kato et al. 1989).

Detailed geological information is unnecessary to detect the presence of ore deposits, but such information might provide additional constraints to support the survey. Bathymetry is particularly important. Using an AUV is effective in this sense because it can acquire bathymetric data during the survey. As an example, for this survey, at least two sites are of interest from the viewpoint of geological information in exploring hydrothermal ore deposits. First, a large scarp structure southwest of the Sunrise deposit with a volcanic ridge (x of approx. 300 m and y of approx. 300 m in Fig. 1c) is a candidate because fluid passageways are likely to form near the edges of scarps and fault structures. Nevertheless, no self-potential anomaly was detected around the observed scarp structure (Fig. 3b). Second, an intensely low-magnetization area ($x < 0$ m and $y < -500$ m in Fig. 1c) discovered by Honsho et al. (2016a) is an interesting area to be surveyed. Honsho et al. (2016a) reported that this low-magnetic anomaly might represent a fluid conduit that forms the Sunrise deposit east of this magnetic low. Nevertheless, no intense self-potential anomaly was detected above this low-magnetization area (Figs. 1c, 3b). This low-magnetization zone and the Sunrise deposit, both showing low magnetization (Honsho et al. 2016a), are indistinguishable based solely on magnetic surveys, but can be distinguished by the present self-potential survey.

The self-potential method can be combined with active electric and electromagnetic surveys that obtain the electrical conductivity structure. Actually, such a combined survey in marine environments has been attempted very recently (Constable et al. 2018). The self-potential survey might be combined easily with these methods, with an electric current source provided properly, because the instrument used for the self-potential method is the same as a receiver unit of the electric/electromagnetic method (e.g., Goto et al. 2013). In other words, electric and electromagnetic surveys record self-potential signals unintentionally. In these active surveys, self-potential signals are obtained as fluctuations in the baseline that might be removed as noise. To obtain self-potential signals from the data of these active surveys, the data should be averaged over a cycle of the active source signal because the cycle comprises an alternating negative and positive current source pair (e.g., Constable et al. 2018; Safipour et al. 2017). Using data obtained from these active surveys, a self-potential signal is useful as a quick-look tool. Then the analysis of the active surveys is used to obtain information about the electrical conductivity structure, but also to obtain a proxy for ore deposits. Again, using an AUV improves the survey efficiency (e.g., Constable et al. 2018).

Self-potential method compared to other geophysical methods

The self-potential method can be compared with some geophysical methods. The self-potential method can obtain information related to redox reactions occurring

around an ore body via the geo-battery mechanism (Sato and Mooney 1960) below the seafloor; other factors that might affect in situ self-potential are discussed in Additional file 2. For the geo-battery to work, a redox boundary is required. In on-land environments, it is a water table below the ground (Sato and Mooney 1960). In marine environments, it could be the seafloor in the absence of sub-seafloor water circulation but it might be situated below the seafloor in the presence of water circulation. This point is crucially important for the marine self-potential method because only visible deposits are targeted in the former case. Completely buried ore deposits can be detected in the latter case.

The observed self-potential data predict the existence of electrical current sources, which might only be determined using this method. Electrical current is not a substance-specific quantity but a quantity depending on the surrounding environment. In this sense, the self-potential has a different characteristic from the magnetic method, as discussed below in this section. Instead, the self-potential responds specifically to the existence of an ore deposit, which is an ideal behavior for exploration. Furthermore, the intensity of the self-potential might be a positive increasing function of the size of an ore body, although it is related not only to the ore body size but also to its shape, chemical composition, and other characteristics.

The magnetic method detects anomalies of magnetization inherent to mineral assemblages, which have been widely used for exploring hydrothermal systems. The most successful magnetic survey related to exploration of hydrothermal deposits was that conducted by Tivey and Johnson (2002), who found circular low-magnetization areas that coincided with the location of active and extinct hydrothermal sites near the Juan de Fuca Ridge axis. These magnetic lows are putatively attributed to the alteration of magnetized minerals into non-magnetized minerals rather than to thermal demagnetization because extinct systems show low magnetization (Tivey and Johnson 2002). However, the detected signals are generally not linked immediately to the presence of the ore deposits because the degree of magnetization depends on the mineral assemblage.

Two contrasting observations, both of which are associated with silicic volcanoes, illustrate the difficulty for interpreting the magnetic anomaly in exploration. First, above the Sunrise deposit associated with a rhyolite volcano, the target of the present study, only a weak magnetization low has been observed (Honsho et al. 2016a). This structure might be influenced by a geological structure inherent to this site and by a fluid flow (alteration) pattern. Second, above another hydrothermal field associated with a dacitic volcano, the Hakurei hydrothermal field of the mid-Okinawa Trough, high magnetization is found that is correlated with hydrothermal mounds (Honsho et al. 2016b). Analyzing the magnetic susceptibility of drilled core samples in this field, Honsho et al. (2016b) argued that the high magnetization is attributable to the existence of pyrrhotite, a sulfide mineral with high magnetization. Moreover, volcanic bodies show high magnetization; fluid conduits show low magnetization (e.g., Honsho et al. 2016b). As a historical fact, before the discovery of the Hakurei hydrothermal field, many observations were conducted with high magnetization around dacitic volcanic bodies, located north of the hydrothermal field (Kato et al. 1989). Consequently, in adopting the magnetic method to the exploration of hydrothermal deposits, geological information serves an important role: it distinguishes observed anomalies of the kinds described above. The self-potential method requires no such information, but it provides some useful constraints. It detects a negative self-potential anomaly above an ore body with either high or low magnetization. It does not respond to a volcanic body or a fluid conduit. Nonetheless, the geomagnetic method is beneficial because magnetization information is related to a substance-specific quantity, particularly when combined with geological and mineralogical information (Honsho et al. 2016b).

The plume method (e.g., Baker et al. 2005; German et al. 2008) might also be applicable to detect information of hydrothermal ore deposits because hydrothermal vents often accompany ore deposits (although the converse is not always true). Active hydrothermal systems discharging high-temperature fluids can be detected by anomalies of temperature, turbidity, and dissolved chemical species; direct effects of hydrothermal fluid on the self-potential are estimated as minor (see Additional file 2). The precise location of hydrothermal vents involving fluid discharges cannot be specified, however, because the discharged fluid is transported by the ambient ocean current. More importantly, plume surveys do not respond directly to signals from ore deposits at or below the seafloor itself, but to the discharged fluid. Consequently, inactive systems cannot be observed to any degree using this method, in principle. This characteristic is common among methods that detect anomalies in discharged hydrothermal fluids such as the redox potential (Eh) (e.g., Baker et al. 2005; German et al. 2008), dissolved chemical species of hydrothermal origin (Fe, Mn, CH_4, etc.) (e.g., Gamo et al. 1996; Shitashima 2010), and acoustic impedance (Kasaya et al. 2015; Nakamura et al. 2015). Although it is coincident with the defect described above, the best aspect of the plume method is its remote nature: the signals can therefore extend far from the source. In the present study, anomalies of turbidity and

temperature were found above the most intense area of the hydrothermal field (Fig. 6), where the self-potential anomalies were detected (Fig. 3b). However, anomalies of turbidity and temperature exist without the presence of self-potential anomalies. The latter type of anomaly might reflect the fluid of the diffused component caused by the ocean current because the locations of the anomalies more or less coincide with depth contour lines. Consequently, although the detection limit of the survey altitude for the plume method is probably higher [e.g., approx. 200 m shown in Baker et al. (2005)] than the self-potential method, the self-potential method can detect the location of hydrothermal ore deposits more specifically than the plume method can.

To summarize, the self-potential method can detect hydrothermal ore bodies more directly than magnetic and plume methods can. The self-potential detects signals from ore bodies directly, whereas the magnetic method detects the degree of alteration caused by ore-forming hydrothermal fluids. The plume method detects hydrothermal fluids that are sometimes spread by the ambient ocean current. No single geophysical method can specify all properties of ore deposits, but combining various methods can elucidate ore deposits better.

Conclusions

We conducted a simultaneous survey of self-potential and turbidity using an AUV at the Sunrise deposit in Myojin Knoll caldera of the Izu-Ogasawara arc, southern Japan. The survey, completed during the daytime, can produce a map of self-potentials extending for a square kilometer with a survey height of approx. 100 m and a survey speed of approx. 2 knots. These results suggest practical upper limits for moderately active hydrothermal fields. During this cruise, we observed a negative self-potential anomaly with amplitude of a few millivolts for a large area: 300 m $\times$ 300 m. The area of self-potential anomaly is consistent with results of a visual survey conducted earlier. Moreover, results show that the self-potential signal exhibits asymmetry along the survey lines. Modeling images revealed a southward-dipping (approx. 60° from vertical) electrical dipole source 30 m below the seafloor. The dipole moment is estimated as approx. 1.4×10^3 A m. This result can be compared with that associated with other hydrothermal fields.

Combining a map of self-potential anomalies with a map of temperature/turbidity anomalies demonstrates that the self-potential method can detect locations of hydrothermal source areas more directly than plume-related methods can. This cruise revealed that the presence of self-potential anomalies does not always correlate with those of turbidity and temperature, which are the direct contributions of hydrothermal plume fluids. Moreover, having precise bathymetry of the target area and an anomaly map of the self-potential, we recognized that the presence of ore deposits is not always correlated with a scarp structure, which is a candidate for the presence of ore deposits. The Sunrise deposit is in fact located at the tip of a scarp structure. The findings presented above can be elucidated only using an AUV.

Additional files

Additional file 1: Fig. A1. Time series of raw data with the range of survey lines. **Fig. A2.** Map view of the dive tracks. **Fig. A3.** Cross-sectional view of results obtained along survey lines oriented E–W. **Fig. A4.** Fitting of the observed electric field by point source inversion along selected survey lines oriented NE–SW. **Fig. A5.** Fitting of the observed electric field by point source inversion along selected survey lines oriented E–W. **Fig. A6.** Results of probability tomography. **Fig. A7.** Fitting of the observed electric field using 2.5-dimensional probability density tomography along selected survey lines.

Additional file 2. Contributions of factors other than the geo-battery affecting in situ self-potential.

Abbreviations

AUV: autonomous underwater vehicle; CTD: conductivity–temperature–depth; DO: dissolved oxygen; DVL: Doppler velocity log; FRP: fiber-reinforced plastics; INS: inertial navigation system; RKF: robust Kalman filter; SSBL: super-short baseline.

Author contributions

TK designed the instrument and conducted observations. YK conducted data analysis and prepared the manuscript and figures. YK and TK discussed the results. All authors read and approved the final manuscript.

Author information

Not applicable.

Author details

[1] International Research Institute of Disaster Science, Tohoku University, 468-1 Aoba, Aoba-ku, Sendai 980-0845, Japan. [2] Japan Agency for Marine–Earth Science and Technology, 2-15 Natsushima-cho, Yokosuka 237-0061, Japan.

Acknowledgements

This study was supported by the *Cross-ministerial Strategic Innovation Promotion Program "Next-generation technology for ocean resources exploration"* launched by the *Council for Science, Technology and Innovation* (CSTI) and managed by *the Japan Agency for Marine–Earth Science and Technology* (JAMSTEC). Data used for this study are available from the authors upon request. We thank the captain and crew of R/V *Kaimei*, Chief Scientist Y. Nakano, and onboard scientists and marine technicians for assisting the observation during the cruise KM16-10. We are grateful to T. Hyakudome for arranging the observation and the AUV team for operating *Jinbei* and to T. Goto for fruitful discussion. The precise bathymetry compiled by C. Honsho was useful for determining our survey lines. We also acknowledge anonymous reviewers for their comments, which have improved the manuscript. Most of the figures were drawn using Generic Mapping Tools software (Wessel et al. 2013).

Competing interests

The authors declare that they have no competing interests.

Availability of data and materials

Data used for this study are available from the authors upon reasonable request (kawada@irides.tohoku.ac.jp, tkasa@jamstec.go.jp).

Consent for publication
Not applicable.

Endnotes
Not applicable.

Ethics approval and consent to participate
Not applicable.

Funding
Not applicable.

Publisher's Note

Received: 1 May 2018 Accepted: 20 August 2018
Published online: 30 August 2018

References

Baker ET, Massoth GJ, Nakamura K-I, Embley RW, de Ronde CEJ, Arculus RJ (2005) Hydrothermal activity on near-arc sections of back-arc ridges: results from the Mariana Trough and Lau Basin. Geochem Geophys Geosyst 6:Q09001. https://doi.org/10.1029/2005GC000948

Beltenev V, Ivanov V, Rozhdestvenskaya I, Cherkashov G, Stepanova T, Shilov V, Davydov M, Laiba A, Kaylio V, Narkevsky E, Pertsev A, Dobretzova I, Gustaytis A, Ye Popova, Ye Amplieva, Evrard C, Moskalev L, Gebruk A (2009) New data about hydrothermal fields on the Mid-Atlantic Ridge between 11°–14°N: 32nd Cruise of R/V Professor Logatchev. Interridge News 18:13–37

Brewitt-Taylor CR (1975) Self-potential prospecting in the deep oceans. Geology 3:541–542. https://doi.org/10.1130/0091-7613(1975)3%3c541:SPITDO%3e2.0.CO;2

Caratori Tontini F, Davy B, de Ronde CEJ, Embley RW, Leybourne M, Tivey MA (2012a) Crustal magnetization of Brothers volcano, New Zealand, measured by autonomous underwater vehicles: geophysical expression of a submarine hydrothermal system. Econ Geol 107:1571–1581. https://doi.org/10.2113/econgeo.107.8.1571

Caratori Tontini F, de Ronde CEJ, Yoerger D, Kinsey J, Tivey M (2012b) 3-D focused inversion of near-seafloor magnetic data with application to the Brothers volcano hydrothermal system, Southern Pacific Ocean, New Zealand. J Geophys Res 117:B10102. https://doi.org/10.1029/2012JB009349

Cherkashev GA, Ivanov VN, Beltenev VI, Lazareva LI, Rozhdestvenskaya II, Samovarov ML, Poroshina IM, Sergeev MB, Stepanova TV, Dobretsova IG, Kuznetsov VY (2013) Massive sulfide ores of the northern equatorial Mid-Atlantic Ridge. Oceanol 53:607–619. https://doi.org/10.1134/S0001437013050032

Constable S, Kowalczyk P, Bloomer S (2018) Measuring marine self-potential using an autonomous underwater vehicle. Geophys J Int 215:49–60. https://doi.org/10.1093/gji/ggy263

Corwin RF (1976) Offshore use of the self-potential method. Geophys Prospect 24:79–90. https://doi.org/10.1111/j.1365-2478.1976.tb00386.x

Filloux JH (1987) Instrumentation and experimental methods for oceanic studies. In: Jacobs JA (ed) Geomagnetism, vol 1. Academic Press, New York

Fiske RS, Naka J, Iizasa K, Yuasa M, Klaus A (2001) Submarine silicic caldera at the front of the Izu-Bonin arc, Japan: voluminous seafloor eruptions of rhyolite pumice. Geol Surv Am Bull 113:813–824. https://doi.org/10.1130/0016-7606(2001)113%3c0813:SSCATF%3e2.0.CO;2

Francis TJG (1985) Resistivity measurements of an ocean floor sulphide mineral deposit from the submersible Cyana. Mar Geophys Res 7:419–437. https://doi.org/10.1007/BF00316778

Fujii M, Okino K, Honsho C, Dyment J, Szitkar F, Mochizuki N, Asada M (2015) High-resolution magnetic signature of active hydrothermal systems in the back-arc spreading region of the southern Mariana Trough. J Geophys Res 120:2821–2837. https://doi.org/10.1002/2014JB011714

Gamo T, Nakayama E, Shitashima K, Isshiki K, Obata H, Okamura K, Kanayama S, Oomori T, Koizumi T, Matsumoto S, Hasumoto H (1996) Hydrothermal plumes at the Rodriguez triple junction, Indian ridge. Earth Planet Sci Lett 142:261–270. https://doi.org/10.1016/0012-821X(96)00087-8

Gee JS, Webb SC, Ridgway J, Staudigel H, Zumberge MA (2001) A deep tow magnetic survey of Middle Valley, Juan de Fuca Ridge. Geochem Geophys Geosyst 2:1059. https://doi.org/10.1029/2001GC000170

German CR, Yoerger DR, Jakuba M, Shank TM, Langmuir CH, Nakamura K (2008) Hydrothermal exploration with the autonomous benthic explorer. Deep Sea Res I 55:203–219. https://doi.org/10.1016/j.dsr.2007.11.004

Goto T, Kasaya T, Imamura N, Mikada H, Takekawa J, Sayanagi K (2013) Electromagnetic survey around the seafloor massive sulfide using autonomous underwater vehicle. In: Proceedings of the 11th SEGJ international symposium, pp 342–345. https://doi.org/10.1190/segj112013-087

Hannington MD, Galley AG, Herzig PM, Petersen S (1998) Comparison of the TAG mound and stockwork complex with Cyprus-type massive sulfide deposits. Proc ODP Sci Res 158:389–415. https://doi.org/10.2973/odp.proc.sr.158.217.1998

Heinson G, White A, Constable S, Key K (1999) Marine self-potential exploration. Explor Geophys 30:1–4. https://doi.org/10.1071/EG999001

Heinson G, White A, Robinson D, Fathianpour N (2005) Marine self-potential gradient exploration of the continental margin. Geophysics 70:G109–G118. https://doi.org/10.1190/1.2057981

Honsho C, Ura T, Kim K (2013) Deep-sea magnetic vector anomalies over the Hakurei hydrothermal field and the Bayonnaise knoll caldera, Izu-Ogasawara arc, Japan. J Geophys Res 118:5147–5164. https://doi.org/10.1002/jgrb.50382

Honsho C, Ura T, Kim K, Asada A (2016a) Postcaldera volcanism and hydrothermal activity revealed by autonomous underwater vehicle surveys in Myojin Knoll caldera, Izu-Ogasawara arc. J Geophys Res 121:4085–4102. https://doi.org/10.1002/2016JB012971

Honsho C, Yamazaki T, Ura T, Okino K, Morozumi H, Ueda S (2016b) Magnetic anomalies associated with abundant production of pyrrhotite in a sulfide deposit in the Okinawa Trough, Japan. Geochem Geophys Geosyst 17:4413–4424. https://doi.org/10.1002/2016GC006480

Hyakudome T, Yoshida H, Ishibashi S, Ochi H, Sawa T, Nakano Y, Watanabe Y, Nakatani T, Sugesawa M, Ohta Y, Watanabe K, Oomika S, Nanbu Y, Komuku T, Matsuura M (2012) Development of AUV for scientific observation. Oceans 2012:1–4. https://doi.org/10.1109/OCEANS.2012.6404892

Iizasa K, Fiske RS, Ishizuka O, Yuasa M, Hashimoto J, Ishibashi J, Naka J, Horii Y, Fujiwara Y, Imai A, Koyama S (1999) A Kuroko-type polymetallic sulfide deposit in a submarine silicic caldera. Science 283:975–977. https://doi.org/10.1126/science.283.5404.975

Jardani A, Revil A (2009) Stochastic joint inversion of temperature and self-potential data. Geophys J Int 179:640–654. https://doi.org/10.1111/j.1365-246X.2009.04295.x

Jouniaux L, Ishido T (2012) Electrokinetics in earth sciences: a tutorial. Int J Geophys 2012:286107. https://doi.org/10.1155/2012/286107

Kaneda Y, Irizuki Y, Yamakita M (2012) Design method of robust Kalman filter via L_1 regression and its application for vehicle control with outliers. Proc IECON 2012:2210–2215. https://doi.org/10.1109/IECON.2012.6388678

Kasaya T, Machiyama H, Kitada K, Nakamura K (2015) Trial exploration for hydrothermal activity using acoustic measurements at the North Iheya Knoll. Geochem J 49:597–602. https://doi.org/10.2343/geochemj.2.0389

Kato Y, Nakamura K, Iwabuchi Y, Hashimoto J, Kaneko Y (1989) Geology and topography in the Izena Hole of the Middle Okinawa Trough—results of diving surveys in 1987 and 1988. JAMSTEC Deep-sea Res 5:163–182 **(in Japanese with English abstract and figure captions)**

Kawada Y, Kasaya T (2017) Marine self-potential survey for exploring seafloor hydrothermal ore deposits. Sci Rep 7:13552. https://doi.org/10.1038/s41598-017-13920-0

Kitagawa G (1993) FORTRAN77 Time-series Programming. Iwanami Syoten, Tokyo **(in Japanese)**

Körner U (1994) Rock magnetic properties of hydrothermally formed iron sulfides from Middle Valley, Juan de Fuca ridge. Proc ODP Sci Res 139:535–542. https://doi.org/10.2973/odp.proc.sr.139.243.1994

Minsley BJ, Sogade J, Morgan HD (2007) Three-dimensional source inversion of self-potential data. J Geophys Res 112:B02202. https://doi.org/10.1029/2006JB004262

Nakamura K, Kawagucci S, Kitada K, Kumagai H, Takai K, Okino K (2015) Water column imaging with multibeam echo-sounding in the mid-Okinawa Trough: implications for distribution of deep-sea hydrothermal vent

sites and the cause of acoustic water column anomaly. Geochem J 49:579–596. https://doi.org/10.2343/geochemj.2.0387
Patella D (1997a) Introduction to ground surface self-potential tomography. Geophys Prospect 45:653–681. https://doi.org/10.1046/j.1365-2478.1997.430277.x
Patella D (1997b) Self-potential global tomography including topographic effects. Geophys Prospect 45:843–863. https://doi.org/10.1046/j.1365-2478.1997.570296.x
Petersen S, Shipboard Scientific Party (2016) Metal fluxes and resource potential at the slow-spreading TAG midocean ridge segment (26°N, MAR)—Blue Mining@Sea. GEOMAR Rept 32. http://oceanrep.geomar.de/34777/1/geomar_rep_ns_32_2016.pdf
Revil A, Jardani A (2013) The self-potential method: theory and applications in environmental geosciences. Cambridge University Press, Cambridge
Revil A, Ehouarne L, Thyreault E (2001) Tomography of self-potential anomalies of electrochemical nature. Geophys Res Lett 28:4363–4366. https://doi.org/10.1029/2001GL013631
Safipour R, Hölz S, Halbach J, Jegen M, Petersen S, Swidinsky A (2017) A self-potential investigation of submarine massive sulfides: Palinuro Seamount, Tyrrhenian Sea. Geophysics 82:A51–A56. https://doi.org/10.1190/geo2017-0237.1
Sato M, Mooney HM (1960) The electrochemical mechanism of sulfide self-potentials. Geophysics 25:226–249. https://doi.org/10.1190/1.1438689
Sato S, Goto T, Kasaya T, Kawada Y, Iwamoto H, Kitada K (2017) Noise reduction method of marine spontaneous electric field data using independent component analysis. Butsuri Tansa 70:42–55. https://doi.org/10.3124/segj.70.42 **(in Japanese with English abstract and figure captions)**
Shitashima K (2010) Evolution of compact electrochemical in situ pH-pCO_2 sensor using ISFET-pH electrode. OCEANS 2010. https://doi.org/10.1109/OCEANS.2010.5663782
Szitkar F, Dyment J, Choi Y, Fouquet Y (2014a) What causes low magnetization at basalt-hosted hydrothermal sites? Insights from inactive site Krasnov (MAR16°38′N). Geochem Geophys Geosyst 15:1441–1451. https://doi.org/10.1002/2014GC005284
Szitkar F, Dyment J, Fouquet Y, Honsho C, Horen H (2014b) Magnetic signature of ultramafic-hosted hydrothermal sites. Geology 42:715–718. https://doi.org/10.1130/G35729.1
Tamura Y, Tatsumi Y (2002) Remelting of an andesitic crust as a possible origin for rhyolitic magma in oceanic arcs: an example from the Izu-Bonin arc. J Petrol 43:1029–1047. https://doi.org/10.1093/petrology/43.6.1029
Tamura Y, Gill JB, Tollstrup D, Kawabata H, Shukuno H, Chang Q, Miyazaki T, Takahashi T, Hirahara Y, Kodaira S, Ishizuka O, Suzuki T, Kido Y, Fiske RS, Tatsumi Y (2009) Silicic magmas in the Izu-Bonin oceanic arc and implications for crustal evolution. J Petrol 50:685–723. https://doi.org/10.1093/petrology/egp017
Tivey MA, Dyment J (2013) The magnetic signature of hydrothermal systems in slow spreading environments. In: Rona PA, Devey CW, Dyment J, Murton BJ (eds) Diversity of hydrothermal systems on slow spreading Ocean Ridges. AGU Monograph:188. American Geophysical Union, Washington, DC. https://doi.org/10.1029/2008gm000773
Tivey MA, Johnson HP (2002) Crustal magnetization reveals subsurface structure of Juan de Fuca Ridge hydrothermal vent fields. Geology 30:979–982. https://doi.org/10.1130/0091-7613(2002)030%3c0979:CMRSSO%3e2.0.CO;2
Tsuru T, Okuda A, No T, Kaneda Y, Tamaki K (2008) Subsurface structure of the Myojin Knoll pumiceous volcano obtained from multichannel seismic reflection data. Earth Planets Space 60:721–726. https://doi.org/10.1186/BF03352820
Urabe T, Maruyama A, Marumo K, Seama N, Ishibashi J (2005) The Archaean Park Project: interactions between microbiological and geological processes in deep-sea hydrothermal vent and sub-vent environments. Oceanogr Jpn 14:129–137. https://doi.org/10.5928/kaiyou.14.129 **(in Japanese with English abstract)**
Urabe T, Ura T, Tsujimoto T, Hotta H (2015) Next-generation technology for ocean resources exploration (Zipangu-in-the-Ocean) project in Japan. OCEANS 2015—Genova. https://doi.org/10.1109/oceans-genova.2015.7271762
Von Herzen RP, Kirklin J, Becker K (1996) Geoelectrical measurements at the TAG hydrothermal mound. Geophys Res Lett 23:3451–3454. https://doi.org/10.1029/96GL02077
Wessel P, Smith WHF, Scharroo R, Luis J, Wobbe F (2013) Generic Mapping Tools: improved version released. EOS Trans AGU 94:409–410. https://doi.org/10.1002/2013EO450001
Yamashita M, Kasaya T, Takahashi N, Takizawa K, Kodaira S (2015) Structural characteristics of the Bayonnaise Knoll caldera as revealed by a high-resolution seismic reflection survey. Earth Planets Space 67:45. https://doi.org/10.1186/s40623-015-0214-2
Yoerger DR, Bradley AM, Jakuba M, German CR, Shank T, Tivey M (2007) Autonomous and remotely operated vehicle technology for hydrothermal vent discovery, exploration, and sampling. Oceanography 20:152–161. https://doi.org/10.5670/oceanog.2007.89